ACS APPLIED MATERIALS & INTERFACES

Research Article

www.acsami.org

Photocatalytic and Dye-Sensitized Solar Cell Performances of {010}-Faceted and [111]-Faceted Anatase TiO_2 Nanocrystals Synthesized from Tetratitanate Nanoribbons

Yi-en Du,[†,‡] Qi Feng,*[,‡] Changdong Chen,[‡] Yasuhiro Tanaka,[‡] and Xiaojing Yang*[,†]

[†]Beijing Key Laboratory of Energy Conversion and Storage Materials, College of Chemistry, Beijing Normal University, Beijing 100875, China

[‡]Department of Advanced Materials Science, Faculty of Engineering, Kagawa University, 2217-20 Hayashi-cho, Takamatsu-shi 761-0396, Japan

Supporting Information

ABSTRACT: The morphology and exposed facet of the anatase-type TiO_2 are very important to improve the photocatalytic activity and photovoltaic performance in dye-sensitized solar cells. In this work, we report the synthesis and the photocatalytic and dye-sensitized solar cell performances of anatase-type TiO_2 single nanocrystals with exposed {010}- and [111]-facets and with various morphologies by using exfoliated tetratitanate nanoribbons as precursors. The precursor nanoribbons were prepared from the exfoliation of the protonated and, subsequently, tetramethylammonium/H^+ ion-exchanged $K_2Ti_4O_9$. The colloidal suspension containing the nanoribbons was hydrothermally heated with a microwave-assistance at temperatures from 120 to 190 °C after pH was adjusted to 0.5−14. The dependence of the crystalline phases on temperature and pH indicated that anatase single phase can be obtained at pH 3−13 whereas temperatures higher than 160 °C. The [111]-faceted nanorod-shaped anatase nanocrystals were formed preferentially at pH ≤ 3, whereas the {010}-faceted anatase nanocrystals with morphologies of rhombic, cuboid, and spindle were preferentially at pH ≥5. The morphology observation revealed that the nanoribbons were transformed to anatase nanocrystals mainly by the topotactic structural transformation reaction accompanied by an Ostwald ripening reaction, and pH of the reaction solution took a critical role in the crystal morphology change. At pH ≤1, the mixture of anatase, rutile, and brookite were obtained at higher temperature conditions. The photocatalytic activity and photovoltaic performance were enhanced in an order of surface without a specific facet < [111]-faceted surface < {010}-faceted surface.

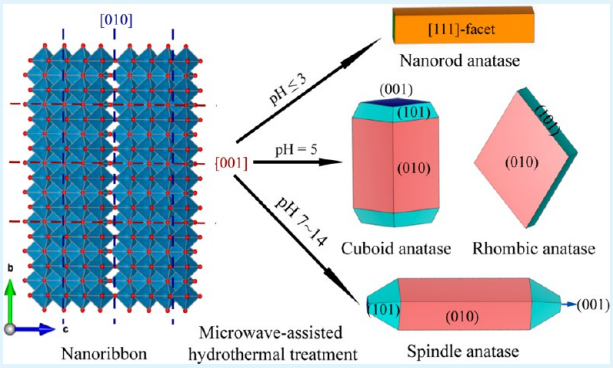

KEYWORDS: *anatase TiO_2, {010}-faceted, [111]-faceted, photocatalysis, dye-sensitized solar cell*

1. INTRODUCTION

Since the discovery of the photochemical splitting of water into hydrogen and oxygen on TiO_2 electrodes in 1972,[1] TiO_2 material has attracted considerable attention from both academic and industrial communities, not only because of its wide application in the field of dye-sensitized solar cells (DSSCs),[2−4] photocatalysis,[5−9] energy storage and conversion,[10,11] electro-chromic and sensing fields,[12] etc., but also because of its low cost, safety, and environmental benignity.[13,14] Photocatalysis is an environmentally friendly and promising technology to enhance the solar to hydrogen energy conversion efficiency and decompose the organic contaminants with the assistance of solar light.[15] For TiO_2 particles, as a wide-band gap semiconducting material, the crystalline phase, crystallinity, crystal size, surface area, pore size distribution, and morphology are found to play an important role in helping to improve the photocatalytic/photovoltaic performance;[16−19] and besides, many factors, such as the heterojunction of anatase/rutile (e.g.TiO_2 (P25) that we will use herein),[20] slow photon enhancement or mutliple scattering enhancement of photocatalytic activity by fabricating 3D ordered photonic film,[21−23] surface and bulk defects,[24] etc., also affect the photocatalytic activity.

TiO_2 crystalline has mainly three polymorphs: anatase, rutile, and brookite, among which anatase has the highest photocatalytic activity.[25−27] To enhance the photocatalytic properties, researchers have devoted substantial efforts to prepare TiO_2 nanocrystals with high crystallinity and large surface area,[28,29] and most recently, intensive attention has been paid to well-exposed high-surface-energy facets.[30−33] The surface energy of anatase nanocrystals is theoretically calculated as 0.44, 0.53, and 0.90 J/m^2 for {101}, {010}, and {001} facets, respectively, on

Received: June 18, 2014
Accepted: August 26, 2014
Published: August 26, 2014

the basis of the Wulff construction.[34,35] Among them, because of the highest energy and superior surface atomic structure, the {001} facet has been accounted as the active facet. Using hydrofluoric acid as a morphology controlling agent, it was reported that with increasing percentage of the exposed {001} facet, the energy conversion efficiency of DSSCs was obviously improved,[36] and large-sized well-defined anatase nanosheets exposed with 98.7% of {001} and 1.3% of {010} facets showed superior photocatalytic performance.[37] In a nonaqueous system, TiO_2 nanosheets and rhombic-shaped nanocrystals TiO_2 with a large percentage of exposed {001} and {010} facets, respectively, were prepared and exhibited conspicuous activities in the photocatalytic degradation of methyl orange.[38] On the other hand, because of the cooperative effects of surface structure and surface electronic structure, the {010} facet exhibits the highest photoreactivity,[39,40] as shown by the uniform anatase microcrystals prepared by using different hydrofluoric acid aqueous under various hydrothermal conditions. Anatase TiO_2 nanorods with dominant reactive {010} facet, prepared by hydrothermal treatment of $Cs_{0.68}Ti_{1.83}O_4/H_{0.68}Ti_{1.83}O_4$ particles, significantly enhanced the photocatalytic conversion of CO_2 into methane.[41] As shown above, the anatase crystals with a dominant {001} or {010} facets are usually prepared in harmful solutions, such as hydrofluoric acid or organic solvents.[15,18] Differently, using TiO_2 nanosheets as precursors, obtained from the exfoliation of layered titanate, {010}-faceted anatase nanocrystals can be synthesized,[42−44] and exhibited high photocatalytic activity and photovoltaic performance.[45,46]

The nanosheets derived from the exfoliation of layered materials are two-dimensional crystals. Besides the exploration of intriguing physicochemical properties, attentions were also paid to the suitability as a building block to create new superlattice materials through, for example, layer-by-layer method or to synthesis materials as a precursor.[47] It has been found that the transformation of TiO_2 nanosheets to {010}-faceted anatase nanocrystals proceeded through in situ topotactic transformation reaction.[42−44] Thus, the structure of the precursor would affect the crystalline phase state and the facet exposure. Through such a reaction, anatase and rutile thin films with preferred orientations along [103] and [110] directions, respectively, were obtained from a layered titanate $H_{1.08}Ti_{1.73}O_4$.[48] In this paper, we report the work by using the precursor of nanoribbons exfoliated from layered tetratitanate. The crystal phases and morphologies of the TiO_2 obtained were different from those obtained through hydrothermal/solvothermal treatments on the protonated tetratitanate.[49−51] Anatase nanocrystals with different exposed facets were controllably achieved, and after tuning the reactive temperature, the nanocrystals with different sizes and shapes were also controllably achieved by microwave-assisted hydrothermal treatment. The possible formation mechanism of the anatase nanocrystals and the photocatalytic activities and photovoltaic performances are investigated. The properties were compared with those of the commercial Degussa P25 TiO_2 (80% anatase and 20% rutile).

2. EXPERIMENTAL SECTION

2.1. Preparation of Tetratitanate Nanoribbon Precursor. Layered potassium tetratitanate fiber $K_2Ti_4O_9$ (KTO) was obtained from Otsuka Chemical Co. Ltd. KTO was converted into a protonic tetratitanate $H_2Ti_4O_9{\cdot}nH_2O$ (HTO) by exchanging K^+ of KTO (10.0 g) in 1 L of 1 mol/L HCl solution under stirring conditions at room temperature for 3 days.[52] The acid solution was replaced daily with a fresh one in order to remove K^+ completely from the compounds. After three cycles of acid exchange, the product was separated from the solution by centrifuging under 8000 rpm for 20 min, washed with copious distilled water three times to remove excess acid, and finally dried using a freeze drier. The obtained HTO sample (4.0 g) was mixed with 40 mL of tetramethylammonium hydroxide (TMAOH) solution (12.5%), purchased from Wako Pure Chemical Industries Ltd., and treated hydrothermally in a 70 mL of Teflon-lined stainless steel vessel at 100 °C for 24 h under stirring conditions to prepare a TMA^+-intercalated tetratitanate compound. And further, the sample was dispersed in 400 mL of distilled water under stirring conditions for 24 h at room temperature. After removal of big particles by filtration, the supernatant obtained was a colloidal suspension.

2.2. Microwave-Assisted Hydrothermal Treatment of Tetratitanate Nanoribbon. After the colloidal solution (40 mL) was adjusted to a desired pH value with a 3 mol/L HCl solution and 1 mol/L TMAOH solution, the solution was placed in an autoclave with an internal volume of 80 mL and the microwave-assisted hydrothermal treatment was performed at a desired temperature for 1.5 h. And then the autoclave was cooled down to room temperature under ambient air. The solid was separated from the solution by centrifugation, followed by rinsing with distilled water several times, and finally dried using a freeze drier. The products obtained are referred as to T*x*-pH*y*, where *x* and *y* are temperature and pH, respectively.

2.3. Physical Analysis. The X-ray diffraction data were collected using a powder X-ray diffractometer of SHIMADZU XRD-6100 equipped with Cu $K\alpha$ radiation (λ = 0.15406 nm) at a scan speed of 5°/min and the accelerating voltage of 40 kV and applied current of 30 mA. The morphology observation was carried out using field-emission scanning electron microscopy (FE-SEM; HITACHI S-90X) at an accelerating voltage of 15 kV and applied current of 10 μA in the dark-field mode after the sample was drop-casted on silicon wafers; and transmission electron microscope (TEM) and selected-area electron diffraction (SAED) were performed on a JEOL (JEM-3010) microscope at an accelerating voltage of 300 kV, after the sample was deposited on a standard copper grid supported carbon film.

The Brunauer−Emmett−Teller (BET) surface areas of the samples were determined by a QUANTACHROMEAUTO-SORB1-MP apparatus using nitrogen gas adsorption at −196 °C after the sample was degassed before the adsorption for 0.5 h at 120 °C.

2.4. Photocatalytic Property. The photocatalytic properties were evaluated through the photodegradation of methylene blue (MB) solution under ultraviolet light irradiation. The TiO_2 nanocrystal sample (50 mg) was placed in an Erlenmeyer flask with an internal volume of 150 mL containing 100 mL of the MB aqueous solution (10 mg/L) and sonicated for 2 h to well-disperse the sample in the solution. Prior to the irradiation, the suspension was magnetically stirred for about 30 min in the dark to approach adsorption/desorption equilibrium between the dye and the TiO_2 nanocrystal surface, and then the suspension was illuminated by a 250 W ultraviolet lamp with an emission wavelength of 365 nm at room temperature, and the lamp located at about 80 cm away from the MB solution while being continuously stirred. At intervals of 20 min, 3 mL of solution was drawn from the suspension and immediately centrifuged to remove the TiO_2 nanocrystal. Degradation efficiency of MB by the photocatalytic reaction was determined by measuring the concentration of MB before and after the ultraviolet lamp irradiation using a TU-1901 spectrophotometer (Beijing Purkinje General Instrument Co. Ltd.). The photodegradation efficiency was calculated according to the following formula[53]

$$D(\%) = \frac{C_0 - C_t}{C_0} 100$$

where D is the photodegradation percentage of MB, and C_0 and C_t the initial and final concentration of a MB solution, respectively.

2.5. Adsorption of N719 Dye on TiO_2 Nanocrystals. Adsorption experiment of dye was carried out by a batch method. A TiO_2 nanocrystal sample (10 mg) was added into an ethanol solution

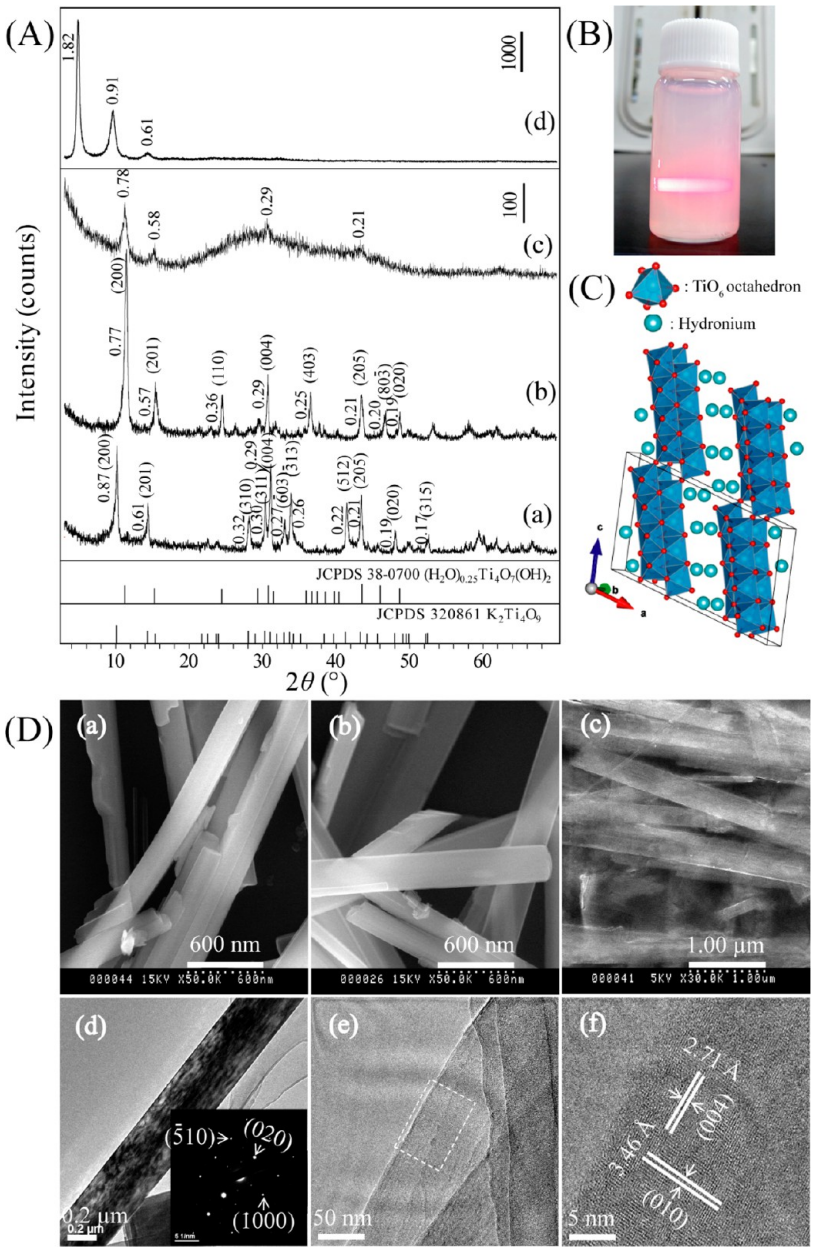

Figure 1. (A) XRD patterns for (a) KTO, (b) HTO, (c) the nanoribbon (the exfoliated tetratitanate), and (d) TMA^+-intercalated tetratitanate samples; (B) Tyndall light scattering of the colloidal suspension; (C) crystal structure of HTO, and (D) FE-SEM images of (a) KTO, (b) HTO, and (c) the nanoribbons, and TEM images of (d) HTO with SAED pattern in the inset and (e, f) the nanoribbons.

(5 mL) of cis-di(thiocyanate) bis (2,2′-bipyridyl-4,4′-dicarboxylate)-ruthenium(II) bis-tetrabutylammonium (N719) dye, purchased from Sigma-Aldrich Co., in a concentration range from 1.0×10^{-5} to 3.0×10^{-4} mol/L and stirred at room temperature for 72 h. After the adsorption, the liquid was separated from the solid by centrifuging under 10000 rpm for 10 min, and then the concentration of the remaining N719 dye in the liquid phase was analyzed using a SHIMADZU UV-2450 spectrophotometer. The amount of the N719 dye adsorbed was determined from the change of dye concentration in ethanol solution before and after the absorption. The TiO_2 nanocrystal samples were calcined at 450 °C for 30 min before the adsorption experiment.

2.6. Photovoltaic Measurements. The TiO_2 electrode of the DSSCs prepared through the doctor-blade method described in the Supporting Information was subjected to photovoltaic measurements. The photocurrent−voltage characteristic curves for the DSSCs were measured using a Hokuto-Denko BAS100B electrochemical analyzer under irradiation with simulated sunlight of AM 1.5 (100 mW/cm^2), using a sunlight simulator (YSS-E40, Yamashita Denso Co., Japan) and a 0.25 cm^2 mask. The thickness of the TiO_2 films was measured using a SURFCOM 480A surface-shape determiner.

3. RESULTS AND DISCUSSION

3.1. Characterization of Nanoribbon Precursor. Figure 1A shows that the basal spacing was changed from 0.87 nm for KTO to 0.77 nm for HTO, and further to 1.82 nm for the TMA^+-intercalated tetratitanate, indicating the protonation of KTO and TMA^+/H^+ ion-exchange occur successfully. The peaks of HTO could be indexed to $(H_2O)_{0.25}Ti_4O_7(OH)_2$ (JCPDS 38−0700), or written as $H_2Ti_4O_9{\cdot}0.25H_2O$. After the colloidal suspension was centrifuged, the nanoribbons sample in wet state was subjected to XRD measurement. Figure 1A(c) indicates some small peaks at d = 0.78, 0.58, 0.29 nm, etc., and a halo in the 2θ range from 20 to 40°. The halo means the

exfoliation of the layered material, corresponding to the Tyndall light scattering (Figure 1B). The small peaks may imply that some nanoribbons restacked to HTO because the basal spacing, 0.78 nm, is very close to that of HTO (Figure 1A(b)). The FE-SEM images show that the nanoribbons (Figure 1D(c)) have several micrometers in length, retaining the profile of the starting material (Figure 1D(a)) and protonated KTO (Figure 1D(b)), but very thin. Figure 1D(d) reveals that the growth direction of HTO coincides with *b*-axis of the crystal. The TEM image of the nanoribbon (Figure 1D(f)) shows two types of lattice fringes, one type with spacing of 3.46 Å, corresponding to the (010) facet of the HTO, perpendicular to the length of the nanoribbons, and another type with spacings of 2.71 Å, corresponding to (004) facet of the HTO nanoribbon, parallel to the length of the ribbons. This reveals that the nanoribbons direction is in the [010]-direction. Because the preferred growth direction is along the *b*-axis of the crystal (Figure 1D(d–f)), the nanoribbons are exfoliated along the direction, retaining well the profile of the crystals. The growth direction of present KTO sample is different from that along *c*-axis reported by Allen et al.[54]

It should be noted here that for the exfoliation, intercalation ion (TMA^+) in the present work is different from those reported, usually tetrabutylammonium ion (TBA^+) and ethylamine solution. Ethylamine solution cannot be alone used as exfoliation reagent, and the direct intercalation of TBA^+ takes longer time than that of TMA^+.[54−56] So we used TMA^+ as the exfoliating agent, in view of it can exfoliate the layered manganese oxide.[57] The basal spacing of 1.82 nm implies the double layers of TMA^+ in the interlayer, since the difference of the summary (1.63 nm) of the thickness of crystallographic nanoribbons (0.57 nm)[58,59] and the height of double layers of TMA^+ (2×0.53 nm)[60] from the basal spacing might be caused by the presence of interlayer water.[61] The double of TMA^+ in the interlayer can be well-explained by the comparison of the area per unit charge, the value of TMA^+ (0.22 nm^2, calculated[60] by supposing the TMA^+ ion as a ball with the diameter of 0.53 nm) is much larger than that of the nanoribbons (0.11 nm^2 = $bc/4$) from the structure model of $H_2Ti_4O_9 \cdot 0.25H_2O$ with lattice parameters a = 0.162, b = 0.374, c = 1.209 nm, β = 105.7°, and Z = 4.

3.2. Formation and Characterization of Anatase Nanocrystals. All the products after the colloidal suspension hydrothermally treated with microwave-assistance in the temperature range from 120−190 °C were subjected to XRD measurement (see the Supporting Information, Figure S1), and Figure 2 shows the typical XRD patterns of the samples. As shown, three TiO_2 polymorphs, anatase, rutile, and brookite were obtained. The dependence of the crystalline phases on temperature and pH are summarized in Table 1. Single anatase phase (tetragonal symmetry, space group $I4_1/amd$, JCPDS No. 21−1272) was generated in the area of temperatures over 150 °C and pH ranged from 3 to 13. The diffraction peaks of anatase crystals became sharper and stronger with the increase of temperatures, implying the increase of crystallinity. A TG-DTA analysis on the samples obtained at pH 5 indicated that those samples treated at higher temperatures have less weight losses and the smaller exothermic peaks emerged at lower temperatures from 323 to 242 °C (see the Supporting Information, Figure S2). The exothermic peaks are produced by the loss of TMA^+ ions, revealing the existence of TMA^+ in the products, and the phase has about 4.6 wt %, much less than in the mixture of anatase and unreacted layered compounds.

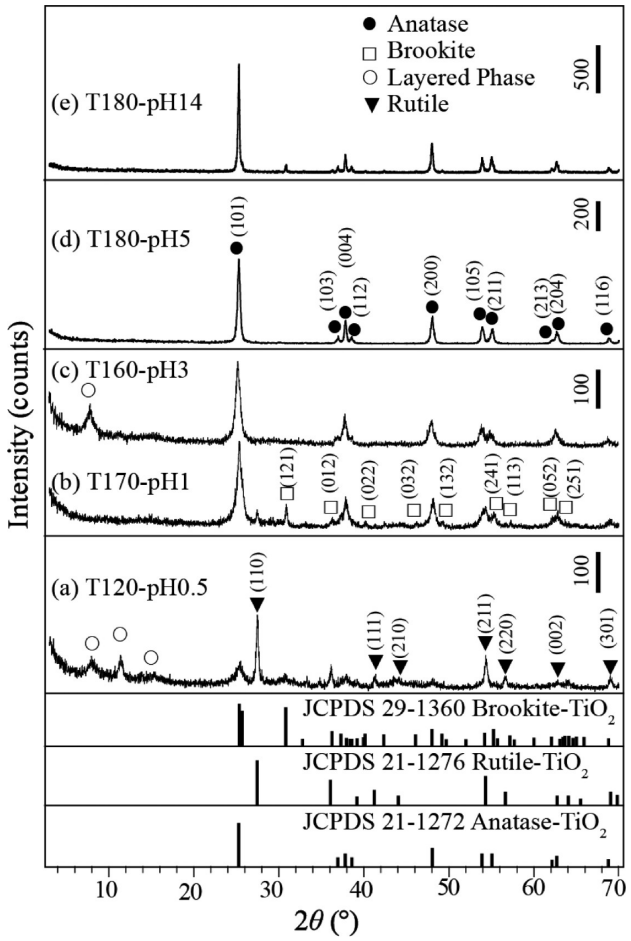

Figure 2. Typical XRD patterns of the samples obtained after hydrothermal treatment.

Table 1. Dependence of the Crystalline Phases on Temperature and pH

	temperature (°C)							
pH	120	130	140	150	160	170	180	190
0.5	A+B+R +L[a]	A+B +R +L	A+B +R	A+B +R	A+B +R	A+B +R	A+B +R	A+B +R
1	L	A+B +R +L	A+B +R +L	A+B +R +L	A+B +R	A+B +R	A+B +R	A+B +R
3	L	A+L	A+L	A+L	A+L	A+L	A	A
5	L	A+L	A+L	A+L	A	A	A	A
7	L	L	L	A+L	A	A	A	A
8	–	L	L	A+L	A	A	A	A
9	–	L	L	A+L	A*	A	A	A
10	–	L	L	A+L	A*	A	A	A
11	L	L	L	A+L	A	A	A	A
12	L	L	L	A+L	A	A	A	A
13	–	L	L	A+L	A	A	A	A
14	–	–	L	L	L	A+B +L	A+B	A+B

[a]A, anatase phase (A*, with a very small amounts of layered phase); B, brookite phase; R, rutile phase; L, unreacted layered compound.

Note that, as shown in Table 1, the nanoribbons undergo stable at temperatures below 140 °C as pH ≥7, and the restacked layered compounds have basal spacing of ~1.15 nm (see the Supporting Information, Figure S1B, C), showing the

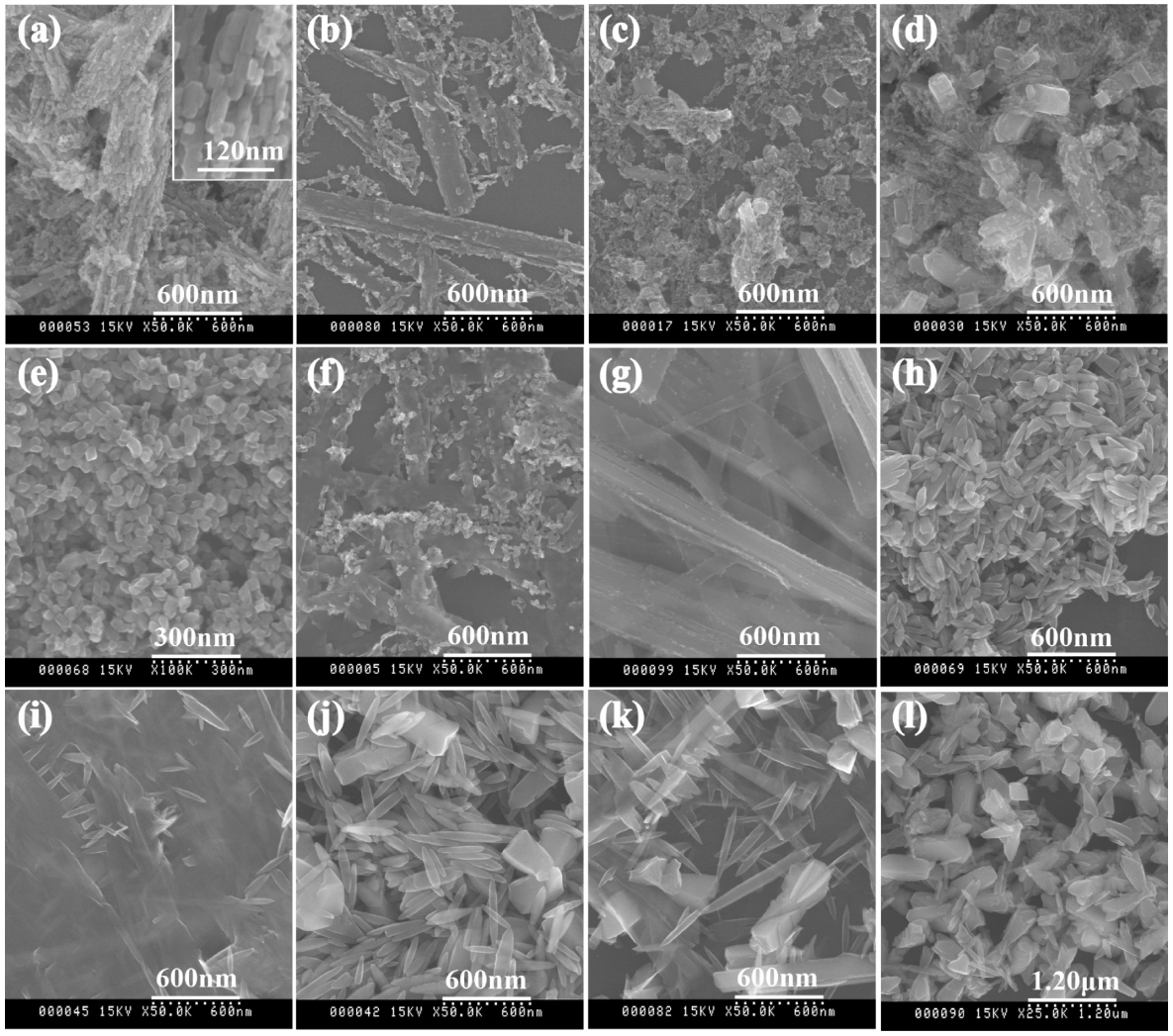

Figure 3. FE-SEM images of (a) T180-pH3, (b) T160-pH3, (c) T160-pH0.5, (d) T180-pH0.5, (e) T180-pH5, (f) T150-pH5, (g) T120-pH5, (h) T180-pH7, (i) T150-pH7, (j) T180-pH12, (k) T150-pH12, and (l) T180-pH14.

monolayer of TMA^+ in the interlayer (0.57 nm of the layer +0.53 nm of TMA^+ = 1.10 nm).

Figure 3 is the FE-SEM images of the selected samples. Nanocrystals were observable for all the samples, and remarkable differences in the morphologies of the anatase nanocrystals. The morphology of the nanocrystals changes from the nanorod (T180-pH3) to cuboid and rhombic (T180-pH5), and to spindle (T180-pH7, T180-pH12) with the increase of pH. Thus, according to the morphology, we separate pH to three ranges, 0.5−3, 5, and 7−14. And to clarify the formation and exposed facets of the differently shaped nanocrystals, detailed observation on the samples obtained at different pH was carried out by TEM and SAED (Figures 4−6).

1. Nanorod-like Anatase. In the range of low pH, the nanorodlike particles of anatase crystals (T180-pH3) constitute a ribbon secondary particle (Figure 3a). The nanorodlike crystals have a size of ∼90 nm in length and ∼20 nm in width (Figure 4a). The lattice spacings of 3.53, 3.51, and 2.30 Å in the TEM image corresponding to the (101), (011), and (112) facets of anatase, respectively, and the angle between the (101) and (011) facets, 82° (Figure 4b) exhibit that the nanocrystals preferentially expose the facets are vertical to [111] crystal zone axis, referred as to [111]-facets. The profile of the secondary particle is very similar to that of T160-pH3 (Figure 3b). For the latter, anatase and unreacted layered phases are found in the XRD pattern (Figure 2c), and in the FE-SEM image, some small nanoparticles on the surface of the nanoribbons are observable (Figure 3b). Correspondingly, in TEM images, cracks are found in the nanoribbon along the *b* axis direction of the HTO structure (Figure 4c), suggesting that the small nanorod particles split from the nanoribbon. The rod crystals with a size of ∼30 nm (∼15 nm) in length and ∼10 nm (∼10 nm) in width are confirmed as the anatase phase from their lattice fringes of the spacing of 3.50 (3.50) and 3.51 Å (3.53 Å), and the angle of 82° between them (Figure 4d,e). The rod extends in the direction vertical to the (011) facet. This direction is the same as that of the *b* axis of the pristine nanoribbon, since the rods split from the nanoribbon (Figure 4c). Thus, a transformation reaction from HTO structure to the anatase structure occurred topotactically. No dislocations are found in the lattice image of the entire particle, revealing that the individual nanorodlike crystals are made of perfectly crystallized anatase TiO_2.[62]

At pH 0.5, for the sample mixture of the three TiO_2 polymorphs, blocky granular, and larger rafterlike (∼800 nm in length and ∼100 nm in width) as well as a lot of small irregular particles were observed in T160-pH0.5 (Figure 3c).

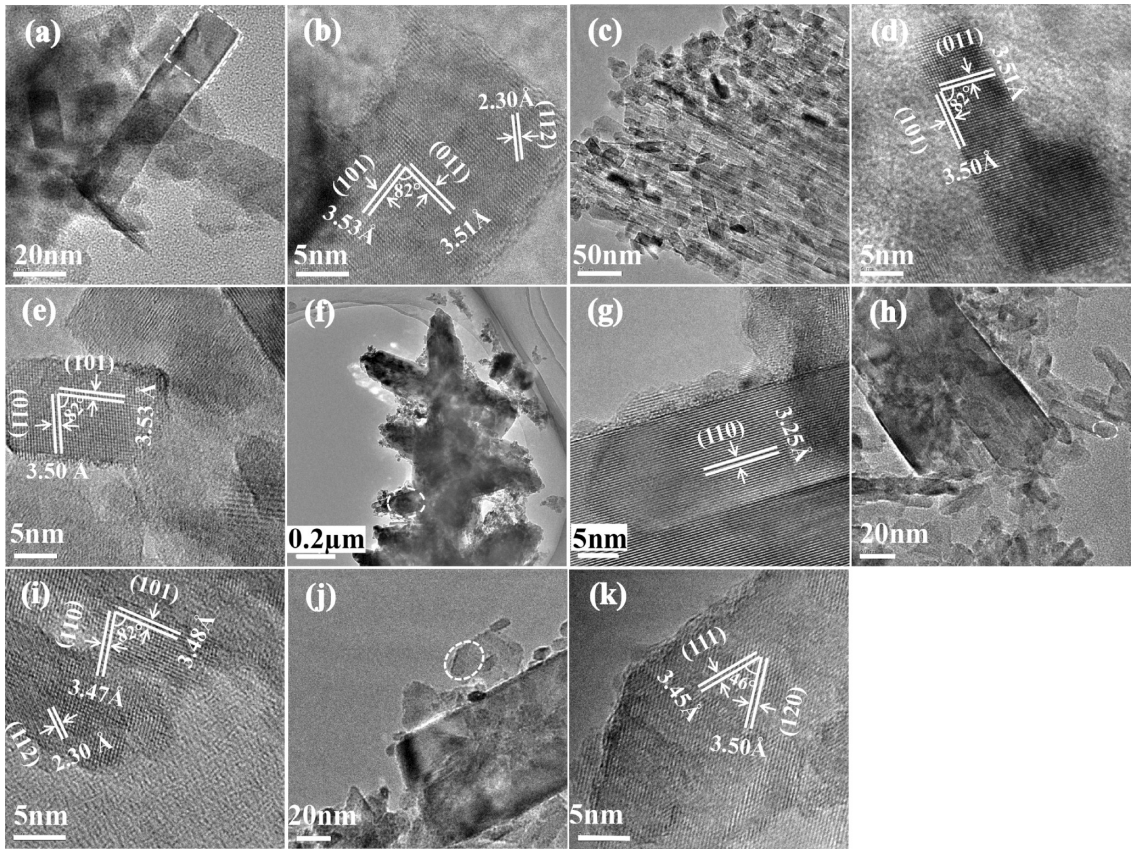

Figure 4. TEM images of (a, b) T180-pH3, (c–e) T160-pH3, (f, g) T160-pH0.5, and (h–k) T180-pH0.5.

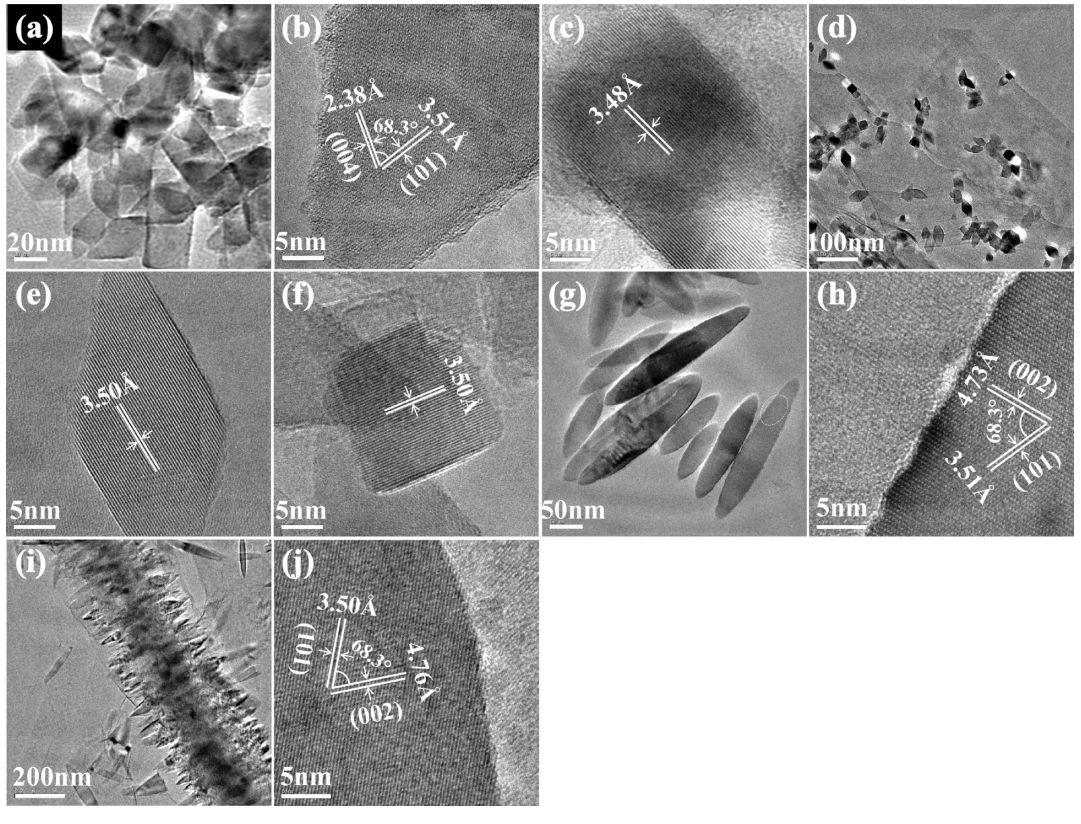

Figure 5. TEM images of (a–c) T180-pH5, (d–f) T150-pH5, (g, h) T180-pH7, and (i, j) T150-pH7.

dx.doi.org/10.1021/am503914q | *ACS Appl. Mater. Interfaces* 2014, 6, 16007–16019

The sizes of the blocky granular and rafterlike particles increase at high temperature for T180-pH0.5 (Figure 3d). The TEM image shows that the rafterlike particles (Figure 4f) with the lattice spacing of 3.25 Å corresponding to the (110) facet (Figure 4g) are rutile phase, whereas the small particles with a nanorodlike morphology are anatase (Figure 4h), as shown by its (112), (011), and (101) facets, respectively, and the angle between the (011) and (101) facets, 82° (Figure 4i). At the same time, some irregular granular particles are also observed (Figure 4j), the spacings of 3.45 and 3.50 Å corresponding to (111) and (120) facets of the brookite phase, respectively, and the angle between the two facets is 46° (Figure 4k), and therefore, the irregular granular particles are brookite. In contrary to the tendency of anatase phase, both the rutile and brookite contents first decrease with the increase of temperature at the range of 140−190 °C, and then increase.

2. Cuboid and Rhombic Anatase. At pH 5, anatase nanocrystals have two morphologies, cuboid and rhombic shapes mainly, respectively (Figures 3e and 5a). The particles have the size of ∼50 nm for T180-pH5. The TEM image (Figure 5b) shows that the lattice spacings of 2.38 and 3.51 Å corresponding to the (004) and (101) facets of anatase TiO_2 phase, respectively, and the 68.3° angle between the (004) and (101) facets agree with the calculated result from the lattice constants of anatase (Tetragonal S.G.: $I4_1/amd$, JCPDS 21−1272, $Z = 4$, $a = 3.7852$ Å, and $c = 9.5139$ Å).[63] This indicates that the basal plane of both the cuboid and rhombic nanocrystals are the {010} facet, vertical to the [010] direction, that is, these anatase nanocrystals preferentially expose the {010} facet on their surfaces. This preferential exposure of anatase was confirmed in the T150-pH5 sample, as shown in Figure 5d−f. Figure 5d shows that the cuboid and rhombic nanocrystals coexist with the unreacted nanoribbons, and the lattice spacing of 3.50 Å shown in images e and f in Figure 5 corresponds to the (101) facets of the anatase phase. Figure 3f shows that the particles with the size of ∼30 nm appear on the surface of multilayer stacking structures of the nanoribbons, which suggests that the nanocrystals may be formed by splitting the nanoribbons. Figure 3g shows the restacked structure of the nanoribbons, implying that the nanoribbons almost unreacted at the lower temperatures.

3. Spindle-Shaped Anatase. In the pH range of 7−14, the spindle-shaped anatase nanocrystals are obtained. For T180-pH7, the spindle-shaped nanocrystals were observed in Figure 3h. The TEM images depict the spindles with ∼200 nm in length and ∼30 nm in width (Figure 5g), and the lattice spacings of 4.73 and 3.51 Å, corresponding to the (002) and (101) facets of anatase, respectively, and the angle between the two facets, 68.3° (Figure 5h). The result indicates the preferential exposure of {010} facets again, although the morphology is different from those of the samples obtained at pH = 5. The observation on the T150-pH7 sample gives the case of coexistence of the anatase spindles and unreacted nanoribbons (Figures 3i and 5i). As shown, the length direction of the spindles is vertical to the *b*-axis of the nanoribbon (Figure 1D(d)). Figure 5i depicts clearly that the spindles split from a pristine nanoribbon, adopting the direction along *c*-axis of the pristine nanoribbon, and Figure 5j reveals that the spindles are anatase with the exposed {010} facets.

For these anatase nanocrystals with different morphologies obtained at different pH mentioned above, we can find the size of the nanocrystals is smaller than that of corresponding ones obtained at the higher temperature (180 °C) (comparing Figure 4a with 4c, 5g with 5i, and 5b/5c with 5e/5f). This result implies that although the formation mechanism is the same for a crystal with certain morphology, but the growth is faster at higher temperatures. The formation process should be an Oswald ripening.[64]

The spindles are bigger in the case of the T180-pH12 sample at pH 12 (Figure 3i), ∼300−600 nm in length and ∼60 nm in width. At the same time, some much bigger irregular nanoparticles with the size ∼300 nm × ∼120 nm are observable (Figure 3j, k). For the irregular particles, because the amount is not high, detailed study was not carried out. Comparing Figure 3j with 3k, however, the size of spindles is smaller than that of T160-pH12 obtained at the lower temperature, which has irregular particles too. This may be attributed to the existence of the irregular particles, as we consider the Ostwald ripening mechanism. On the spindle (Figure 6a), the SAED pattern

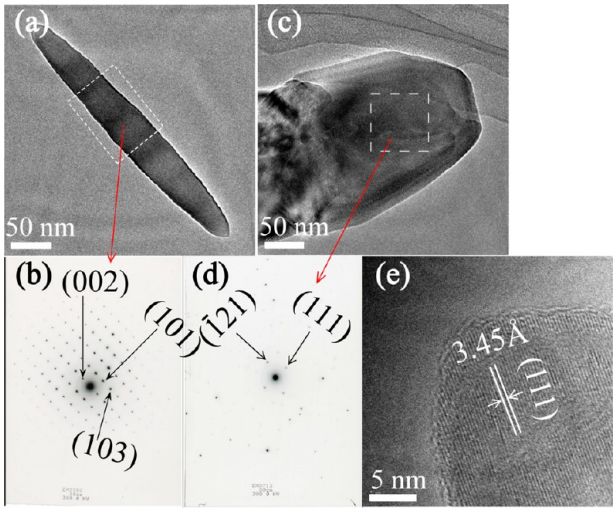

Figure 6. TEM images and SAED patterns of (a, b) T180-pH12 and (c−e) T190-pH 14.

(Figure 6b) confirms that the crystalline is crystal anatase phase, and the exposed facets are {010}. The T190-pH14 sample has anatase as main phase and brookite as minor phase, as shown in the XRD pattern (see the Supporting Information, Figure S1C(g)). Thus, the thickened spindles in the large amount observed in FE-SEM (Figure 3l) are anatase. Furthermore, the plate-shaped particles with an irregular profile (Figure 6c) are confirmed by the SAED pattern (Figure 6d) and TEM image (Figure 6e) to be brookite. The TEM image reveals that the plate-shaped particle shows lattice image with a lattice spacing of 3.45 Å that corresponds to (111) facet of brookite phase (Figure 6e).

3.3. Surface Area and Particle Size. For the nanocrystals of anatase phase obtained at 180 °C, the BET specific surface areas were measured and shown in Table 2. As shown, the specific surface area (S_{BET}) decreases with the increase of pH. This means that the crystalline size increases at high pH, even though the morphology changes. Table 2 also gives the crystallite sizes. The FE-SEM image of P25 and nanoparticle size distributions measured from enlarged photograph of FE-SEM images are shown in Figure S4 in the Supporting Information. The samples of P25, T180-pH3, and T180-pH5 have narrow particle size distributions compare to the T180-pH7 and T180-pH12. As expected, the size increases as pH increases.

Table 2. Characteristics for P25 Particle and the TiO_2 Nanocrystals

sample	phase	morphology	$D_{FE\text{-}SEM}$ [a] (nm)	$D_{(101)}$ [b] (nm)	S_{BET} (m^2/g)
P25	anatase/ rutile	granular	28	20	52.5
T180-pH3	anatase	nanorod	44	19	41.8
T180-pH5	anatase	cuboid/ rhombic	50	27	32.5
T180-pH7	anatase	spindle	148	38	24.6
T180-pH12	anatase	spindle	332	54	18.6

[a]Size of the longest growth direction in FE-SEM images measured using software.[66] [b]Average crystalline size calculated by applying the Scherrer equation[67] to the (101) plane at $2\theta \approx 25.3°$, and k was set as 0.94 without consideration the crystal shape.

3.4. Crystal Shape Simulation and Schematic Presentation of the Structural Transformation. For each morphology of the anatase crystals, simulations were carried out using the VESTA software.[65] According to the results of the HR-TEM/SAED observation, the indices of anatase lattice planes ((101), (001), and (100)) including a preferentially exposed facet (010) and the relative ones were given as parameters into the software by a trial-and-error method, until the morphology obtained was very similar to the observed one. As shown in Figure 7, the results agree well with the observed morphologies.

According to the discussion above, a schematic presentation was proposed to show the transformation reactions (Figure 7). The fibrous particles of the TMA^+-intercalated layered structure are exfoliated into elementary host nanoribbons. The reaction of the transformation from the nanoribbon to TiO_2 proceeds as eq 1.

$$(Ti_4O_9)^{2-} = 4TiO_2 + O^{2-} \quad (1)$$

where the $(Ti_4O_9)^{2-}$ is the chemical formula of $[TiO_6]$ formed layer framework of the nanoribbon host. The cations of TMA^+ and H_3O^+ locate, to balance the negative charge, on the surface. The release of oxygen ion (or the dehydration process) would destruct the framework. Because the transformation is an in situ topotactic transformation reaction, as previously observed for a system,[68] the destruction of the framework would show as splitting at certain lattice planes of the pristine crystal, depending upon pH. This is reasonable for the FE-SEM observation that the cracks in the nanoribbon occur along the [010]-direction of the HTO in the pH range of 0.5−3, and along [001]-direction in the range of 7−14, as shown in the FE-SEM images of Figure 7. The morphology of cuboid and rhombic anatase obtained at pH 5 may be explained as due to the splits along both the two directions. Splitting of the framework at the low pH range possibly takes place at the oxygen atoms corner-shared by two $[TiO_6]$ octahedrons along the b-axis ([010]-direction of the anatase) rather than those edge sharing oxygen atoms. But at higher pH, both kinds of oxygen atoms are considered to release, breaking the framework. The splitting in different directions and difficulty/easiness maybe results in the different fragments in size. This could be used to explain the fact that the size of the anatase increases with increasing pH, under the same temperature and time interval. Because the transformation reaction accompanied by an Ostwald ripening growth of the formed crystal, as mentioned above, the morphology of the precursor changes to differently shaped anatase.

3.5. Photocatalytic Activity. For TiO_2 nanocrystals obtained, the photodegradation experiments of methylene blue (MB) dye were carried out, and compared with the commercially available TiO_2, Degussa P25. Figure 8 shows the time-dependent photodegradation profiles of MB in the presence and absence of TiO_2 nanocrystals samples under ultraviolet irradiation. The corresponding absorption spectra of a methylene blue solution degraded under UV light irradiation are provided in Figure S4 in the Supporting Information. The degradation efficiency of MB at 120 min, increased in an order of 86% (P25), 90% (T180-pH12), 94% (T180-pH3), 96% (T180-pH7), and 99% (T180-pH5). Two factors, the exposed facet and the specific surface area, influence on the efficiency, but the former is the bigger impact. Thus, the samples with exposed {010} facets exhibit the higher photocatalytic activity

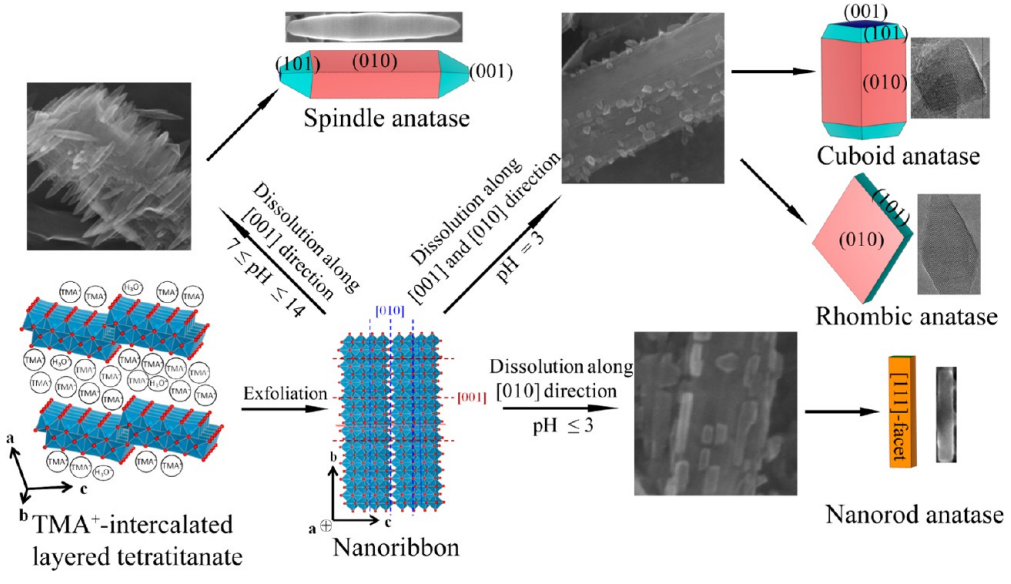

Figure 7. Simulated crystalline shapes and schematic representation of the formation reactions for anatase TiO_2 nanocrystals at different pH.

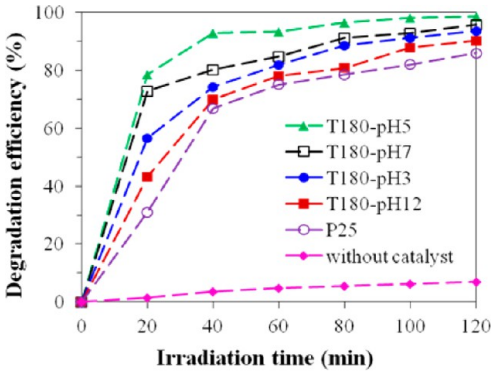

Figure 8. Time-dependent photodegradation profiles of MB in the presence and absence of TiO_2 nanocrystals samples under ultraviolet irradiation.

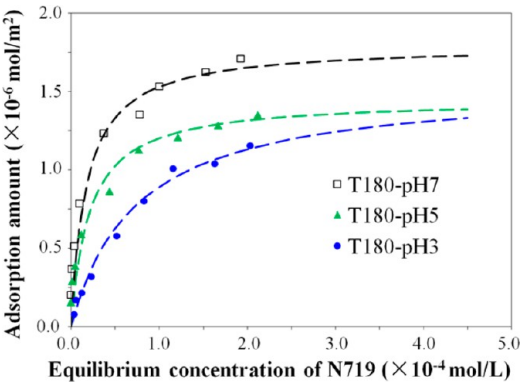

Figure 9. Adsorption isotherms for N719 dye on TiO_2 nanocrystals.

than the commercial P25 without specific facet on the surface. The result is accordance with those of the literature.[41,69] Among the samples with {010} facet, the photocatalytic activity increases with the increase of S_{BET} (Table 2).

The photocatalytic activity in an order of P25 < T180-pH3 < T180-pH5, is the inverse of the S_{BET} value order. This implies that the photocatalytic activity of different exposed facets is in an order of surface without specific facet < [111]-faceted surface < {010}-faceted surface. To characterize the photocatalytic activity of crystal surface, we estimated the reaction rate of MB per surface area. The degradation ratios at 120 min were 0.97, 0.78, 0.47, 0.45, and 0.33 mg(MB)/m^2 for T180-pH12, T180-pH7, T180-pH5, T180-pH3, and P25, respectively. This result reveals that the surface photocatalytic activity in an order of T180-pH12 > T180-pH7 > T180-pH5 > T180-pH3 > and P25, agree with the order of {010}-faceted surface > [111]-faceted surface > surface without specific facet.

3.6. Adsorption Behavior of N719 Dye. The behavior of the dye molecule loaded on various TiO_2 nanocrystals exerts a profound influence on the application of the nanocrystals in DSSCs. The adsorption amount of dye onto TiO_2 sample (mol/g) is strongly dependent on S_{BET}. To more clearly understand the situation of the dye molecules adsorbed on the crystal surface, we present the dye adsorption amount as per S_{BET} of the sample that corresponds to dye adsorption density on the crystal surface. The adsorption amount enhanced with the increase in dye concentration until it reached a saturation value.

Figure 9 is result of the N719 dye adsorption isotherm experiments carried out on the T180-pH3, T180-pH5, and T180-pH7 samples. From these data, the isotherm curves were calculated according to the Langmuir-type isotherm equation linear formula,[70]

$$\frac{C}{\Gamma} = \frac{1}{\Gamma_{max} K_{ad}} + \frac{C}{\Gamma_{max}} \quad (2)$$

where Γ is the N719 adsorption amount (mol/m^2); C, the equilibrium concentration (mol/L); Γ_{max}, the saturated (maximum) adsorption amount (mol/m^2); and K_{ad}, the adsorption equilibrium constant (L/mol). The parameters are given in Table 3 and the curves are shown in Figure 9. The curves agree well with the experimental result, indicating that the N719 dye adsorption on the crystal surface is monolayer adsorption.

The adsorption toward N719 of the three samples is markedly different. The Γ_{max} value increases in the order of T180-pH5, T180-pH3, and T180-pH7, whereas K_{ad} is in an order of T180-pH3 < T180-pH5 < T180-pH7. Both Γ_{max} and K_{ad}, indicating respectively the adsorption density and adsorption binding with the dye molecules, are highest for the surface of T180-pH7, whereas the T180-pH3 sample has the lowest K_{ad}. This result reveals the N719 dye adsorption on [111]-facet is weaker than that on {010}-facet. In the {010}-faceted anatase samples, K_{ad} of T180-pH5 is smaller than that of T180-pH7, which may be due to increases in {010}-facet percentage on the crystal surface and crystallinity of the surface.[71]

3.7. Photovoltaic Performance of DSSCs. It was reported that the TiO_2 film thickness is one of the dominant factors affecting the performance parameters of the DSSCs, such as, the short-circuit photocurrent density (J_{sc}), the open circuit voltage (V_{oc}), and the fill factor (FF).[73] Thus, we fabricated photoanodes with different thickness to optimize the photovoltaic performance of DSSCs using T180-pH3, T180-pH5, T180-pH7, and P25 samples. The short-circuit photocurrent density profiles plotted vs the film thickness are displayed in Figure 10a. The current densities had the similar trend with the increase of the film thickness for all the samples: they first increase with the film thickness, and then flatten out, when the film is beyond a certain thickness with a slight decline. More dye will be absorbed on the surface of the photoanodes with the increase of the film thickness, which is expected to enhance the current density of DSSCs. However, the charge recombination between the electrons injected from the excited dye to the conduction band of the TiO_2 film and the I_3^- ions in the electrolyte will become more serious with increasing of the film thickness, which is extremely disadvantageous to electron collection on the back contact, thus limiting continuous increase of current density.[74] The T180-pH3, T180-pH5, T180-pH7, and P25 samples exhibit the maximum J_{sc} values at the TiO_2 film thicknesses around 16, 14, 17, and 18 μm, respectively.

Contrary to the tendency of the current densities, the open circuit voltage decreased linearly with an increase in the film thickness (Figure 10b). The decrease in the open circuit voltage can be explained as a consequence of increased charge recombination and restricted mass transport in thicker films.[73] The V_{oc} of T180-pH5 was higher than that of other samples with the same film thickness. The fill factor also decreased with the increase of the film thickness (Figure 10c). The increased charge recombination also causes the decrease of

Table 3. N719 Dye-Adsorption Parameters on the TiO_2 Nanocrystals

sample	K_{ad} (L/mol)	Γ_{max} (mol/m^2)	correlation coefficient	$\Gamma_{0.3}$ (mol/m^2)	N_{dye}[a] (number/nm^2)
T180-pH3	1.36×10^4	1.55×10^{-6}	0.966	1.24×10^{-6}	0.75
T180-pH5	4.82×10^4	1.45×10^{-6}	0.995	1.36×10^{-6}	0.82
T180-pH7	5.76×10^4	1.79×10^{-6}	0.995	1.70×10^{-7}	1.02

[a]Calculated[72] from N_{dye}(number/nm^2) = Γ[mol/m^2] × N_A(number/mol) × 10^{-18} at 0.3 mmol/L of N719.

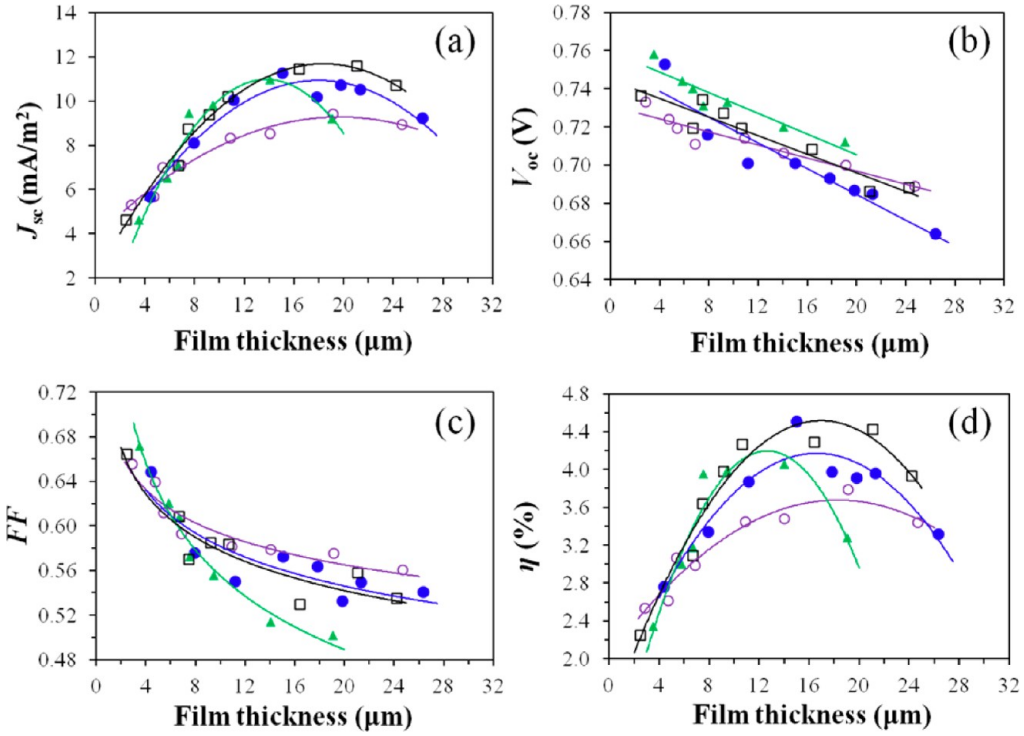

Figure 10. Dependence of the (a) short-current density (J_{sc}), (b) open circuit voltage (V_{oc}), (c) fill factor (*FF*), and (d) power conversion efficiency (η) on film thickness (●, T180-pH3; ▲, T180-pH5; □, T180-pH7; ○, P25).

FF. The power conversion efficiency (η) had the similar trend to J_{sc} with the increase of film thickness for all the samples: with increasing film thickness, η values first increase, achieve a maximum, and then decrease (Figure 10d). The T180-pH3, T180-pH5, T180-pH7, and P25 samples exhibit the maximum η values at the TiO_2 film thicknesses around 16, 14, 17, and 18 μm, respectively, which correspond to their maximum J_{sc} values.

For the highest J_{sc} (maximum η), the photocurrent−voltage characteristic curves of the DSSCs are presented in Figure 11. The corresponding photovoltaic parameters are listed in Table 4. The J_{sc} and η values increase in the same order of P25, T180-pH3, T180-pH5, and T180-pH7, namely, η is strongly dependent on the J_{sc}; whereas the V_{oc} and *FF*, in an order of T180-pH3 < P25 < T180-pH7 < T180-pH5 and an order of T180-pH5 = T180-pH7 < T180-pH3 < P25, respectively. It has reported that there are relationships between the DSSC cell parameters and the sensitizer dye adsorption parameters; the J_{sc} increases with increasing K_{ad}, V_{oc} increases with increasing adsorption density on TiO_2 surface, and P25 has the N719 dye adsorption parameters of $K_{ad} = 9.3 \times 10^3$ L/mol and $\Gamma_{0.3} = 7.4 \times 10^{-7}$ mol/m^2.[71] In the present study, the J_{sc} increasing order agrees also with the K_{ad} order of P25 < T180-pH3 < T180-pH5< T180-pH7 (Table 3). A large value of K_{ad}, meaning a strong binding strength between the dye and TiO_2 surface, would increase the injection rate of excited photoelectrons from the N719 dye molecule into the TiO_2 surface, resulting in the enhancement of the J_{sc}.[45,75] The order of V_{oc} T180-pH3 < P25 < T180-pH7 < T180-pH5 is slightly different from the dye adsorption density of $\Gamma_{0.3}$ order of P25 < T180-pH3 < T180-pH5 < T180-pH7, which may be due to the different TiO_2 film thickness and TiO_2 particle size. The thicker film and smaller particle size of TiO_2, the larger surface area, as causes larger the charge recombination at interface between TiO_2 surface and electrolyte solution, therefore, resulting low V_{oc} value.[76]

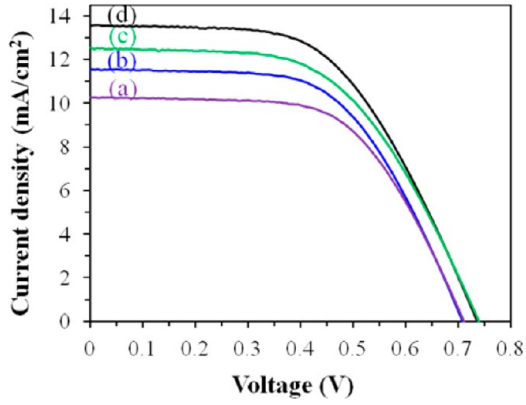

Figure 11. Photocurrent−voltage characteristic curves of DSSCs prepared using (a) P25, (b) T180-pH3, (c) T180-pH5, and (d) T180-pH7.

Table 4. Photovoltaic Parameters of DSSCs Based on Different TiO_2 Photoanodes

electrode	film thickness (μm)	J_{sc} (mA/cm^2)	V_{oc} (V)	FF	η (%)
P25	16.6	10.3	0.711	0.600	4.37
T180-pH3	15.9	11.5	0.708	0.580	4.74
T180-pH5	13.8	12.6	0.739	0.548	5.09
T180-pH7	16.4	13.6	0.736	0.548	5.48

Although reducing the charge recombination could enhance the *FF* of DSSCs, it is also affected by other factors, such as the conductivity of the TiO_2 film, which is independent of the dye-adsorption.[77]

The T180-pH7 sample exhibits the highest η value, because of its highest J_{sc} and relatively higher V_{oc}. The {010}-faceted anatase nanocrystals (T180-pH5 and T180-pH7) exhibit higher J_{sc} than the [111]-faceted sample (T180-pH3), and much higher J_{sc} than without specific facet nanocrystals (P25).

4. CONCLUSIONS

Because of the topotactic transformation from the precursor to TiO_2 nanocrystals, the morphology and structure depend on pH as well as temperature of the microwave-assisted hydrothermal treatment. The tetratitanate nanoribbons lead to, preferentially, the formation of [111]-faceted nanorod-shaped anatase crystals under stronger acidic conditions of pH $\leq$3, and the {010}-faceted anatase nanocrystals with rhombic and cuboid morphology at pH 5, and spindle-shape at pH 7−14. The photocatalytic activity of these anatase nanocrystals increased in the order of surface without specific facet < [111]-faceted surface < {010}-faceted surface. The same enhancement order was also found for the DSSC performance, corresponding to the binding strength of the N719 dye on the TiO_2 surface.

■ ASSOCIATED CONTENT

Supporting Information

Details of fabrication of DSSCs; XRD patterns of the samples obtained by microwave-assisted hydrothermal treatment of tetratitanate nanoribbons at various temperatures and pH values conditions; TG-DTA curves of the samples obtained at pH 5; FE-SEM image of P25 TiO_2 and particles size distributions of P25, T180-pH3, T180-pH5, T180-pH7, and T180-pH12; and absorption spectra of a methylene blue solution degraded under UV light irradiation for 120 min. This material is available free of charge via the Internet at http://pubs.acs.org.

■ AUTHOR INFORMATION

Corresponding Authors

*E-mail: feng@eng.kagawa-u.ac.jp. Fax: +81-87-864-2438. Tel: +81-87-864-2402.

*E-mail: yang.xiaojing@bnu.edu.cn. Fax: +86-10-5880-2075. Tel: +86-10-5880-2960.

Notes

The authors declare no competing financial interest.

■ ACKNOWLEDGMENTS

This work was supported by the National Science Foundation of China (Grant 51272030), and by Grants-in-Aid for Scientific Research (B) (Grant 23350101) from Japan Society for the Promotion of Science and Kagawa University. We thank Dr. Yoji Makita of the National Institute of Advanced Industrial Science and Technology, Takamatsu, Japan, for beneficial discussions on the TEM results.

■ REFERENCES

(1) Fujishima, A.; Honda, K. Electrochemical Photolysis of Water at a Semiconductor Electrode. *Nature* **1972**, *238*, 37−38.

(2) O'Regan, B.; Grätzel, M. A Low-Cost, High-Efficiency Solar Cell Based on Dye-Sensitized Colloidal TiO_2 Films. *Nature* **1991**, *353*, 737−740.

(3) Gao, F. F.; Wang, Y.; Shi, D.; Zhang, J.; Wang, M. K.; Jing, X. Y.; Humphry-Baker, R.; Wang, P.; Zakeeruddin, S. M.; Grätzel, M. Enhance the Optical Absorptivity of Nanocrystalline TiO_2 Film with High Molar Extinction Coefficient Ruthenium Sensitizers for High Performance Dye-Sensitized Solar Cells. *J. Am. Chem. Soc.* **2008**, *130*, 10720−10728.

(4) Xie, F. X.; Cherng, S.-J.; Lu, S. M.; Chang, Y.-H.; Sha, W. E. I.; Feng, S.-P.; Chen, C.-M.; Choy, W. C. H. Functions of Self-Assembled Ultrafine TiO_2 Nanocrystals for High Efficient Dye-Sensitized Solar Cells. *ACS Appl. Mater. Interfaces* **2014**, *6*, 5367−5373.

(5) Linsebigler, A. L.; Lu, G.; Yates, J. T., Jr. Photocatalysis on TiO_2 Surfaces: Principles, Mechanism, and Selected Results. *Chem. Rev.* **1995**, *95*, 735−758.

(6) Tan, L. K.; Kumar, M. K.; An, W. W.; Gao, H. Transparent, Well-Aligned TiO_2 Nanotube Arrays with Controllable Dimensions on Glass Substrates for Photocatalytic Applications. *ACS Appl. Mater. Interfaces* **2010**, *2*, 198−503.

(7) Hsiao, Y.-C.; Wu, T.-F.; Wang, Y.-S.; Hu, C.-C.; Huang, C. Evaluating the Sensitizing Effect on the Photocatalytic Decoloration of Dyes Using Anatase-TiO_2. *Appl. Catal., B* **2014**, *148−149*, 250−257.

(8) Dinh, C. T.; Yen, H.; Kleitz, F.; Do, T. O. Three-Dimensional Ordered Assembly of Thin-Shell Au/TiO_2 Hollow Nanospheres for Enhanced Visible-Light-Driven Photocatalysis. *Angew. Chem., Int. Ed.* **2014**, *53*, 6618−6623.

(9) Yu, S. L.; Liu, B. C.; Wang, Q.; Gao, Y. X.; Shi, Y.; An, X. T.; Liu, L. X.; Zhang, J. Ionic Liquid Assisted Chemical Strategy to TiO_2 Hollow Nanocube Assemblies with Surface-Fluorination and Nitridation and High Energy Crystal Facet Exposure for Enhanced Photocatalysis. *ACS Appl. Mater. Interfaces* **2014**, *6*, 10283−10295.

(10) Park, K.; Zhang, Q. D. F.; Myers, D.; Cao, G. Z. Charge Transport Properties in TiO_2 Network with Different Particle Sizes for Dye Sensitized Solar Cells. *ACS Appl. Mater. Interfaces* **2013**, *5*, 1044−1052.

(11) Sun, W. W.; Peng, T.; Liu, Y. M.; Yu, W. J.; Zhang, K.; Mehnane, H. F.; Bu, C. H.; Guo, S. S.; Zhao, X.-Z. Layer-by-Layer Self-Assembly of TiO_2 Hierarchical Nanosheets with Exposed {001} Facets As an Effective Bifunctional Layer for Dye-Sensitized Solar Cells. *ACS Appl. Mater. Interfaces* **2014**, *6*, 9144−9149.

(12) Chen, D. H.; Huang, F. Z.; Cheng, Y. B.; Caruso, R. Mesoporous Anatase TiO_2 Beads with High Surface Areas and Controllable Pore Sizes: A Superior Candidate for High-Performance Dye-Sensitized Solar Cells. *Adv. Mater.* **2009**, *21*, 2206−2210.

(13) Nam, S. H.; Shim, H. S.; Kim, Y.-S.; Dar, M. A.; Kim, J. K.; Kim, W. B. Ag or Au Nanoparticle-Embedded One-Dimensional Composite TiO_2 Nanofibers Prepared via Electrospinning for Use in Lithium-Ion Batteries. *ACS Appl. Mater. Interfaces* **2010**, *2*, 2046−2052.

(14) Liu, J. H.; Chen, J. S.; Wei, X. F.; Lou, X. W.; Liu, X. W. Sandwich-Like, Stacked Ultrathin Titanate Nanosheets for Ultrafast Lithium Storage. *Adv. Mater.* **2011**, *23*, 998−1002.

(15) Ouyang, S. X.; Tong, H.; Umezawa, N.; Gao, J. Y.; Li, P.; Bi, Y. P.; Zhang, Y. J.; Ye, J. H. Surface-Alkalinization-Induced Enhancement of Photocatalytic H_2 Evolution over $SrTiO_3$-Based Photocatalysts. *J. Am. Chem. Soc.* **2012**, *134*, 1974−1977.

(16) Hagfeldt, A.; Grätzel, M. Light-Induced Redox Reactions in Nanocrystalline Systems. *Chem. Rev.* **1995**, *95*, 49−68.

(17) Morgado, E., Jr.; dr Abreu, M. A. S.; Moure, G. T.; Marinkovic, B. A.; Jardium, P. M.; Araujo, A. S. Characterization of Nanostructured

Titanates Obtained by Alkali Treatment of TiO_2-Anatases with Distinct Crystal Sizes. *Chem. Mater.* **2007**, *19*, 665−676.
(18) Zhou, W. J.; Liu, H.; Wang, J. Y.; Liu, D.; Du, G. J.; Cui, J. J. Ag_2O/TiO_2 Nanobelts Heterostructure with Enhanced Ultraviolet and Visible Photocatalytic Activity. *ACS Appl. Mater. Interfaces* **2010**, *2*, 2385−2392.
(19) Yan, X. D.; Feng, L.; Jia, J. G.; Zhou, X. W.; Lin, Y. Controllable Synthesis of Anatase TiO_2 Crystals for High-Performance Dye-Sensitized Solar Cells. *J. Mater. Chem. A* **2013**, *1*, 5347−5352.
(20) Zhang, J.; Xu, Q.; Feng, Z. C.; Li, M. J.; Li, C. Importance of the Relationship between Surface Phases and Photocatalytic Activity of TiO_2. *Angew. Chem., Int. Ed.* **2008**, *47*, 1766−1769.
(21) Chen, J. I. L.; Freymann, G. V.; Choi, S. Y.; Kitaev, V.; Ozin, G. A. Amplified Photochemistry with Slow Photons. *Adv. Mater.* **2006**, *18*, 1915−1919.
(22) Li, Y. Z.; Kunitake, T.; Fujikawa, S. Efficient Fabrication and Enhanced Photocatalytic Activities of 3D-Ordered Films of Titania Hollow Spheres. *J. Phys. Chem. B* **2006**, *110*, 13000−13004.
(23) Xie, H.; Li, Y. Z.; Jin, S. F.; Han, J. J.; Zhao, X. J. Facile Fabrication of 3D-Ordered Macroporous Nanocrystalline Iron Oxide Films with Highly Efficient Visible Light Induced Photocatalytic Activity. *J. Phys. Chem. C* **2010**, *114*, 9706−9712.
(24) Kong, M.; Li, Y. Z.; Chen, X.; Tian, T. T.; Fang, P. F.; Zheng, F.; Zhao, X. J. Tuning the Relative Concentration Ratio of Bulk Defects to Surface Defects in TiO_2 Nanocrystals Leads to High Photocatalytic Efficiency. *J. Am. Chem. Soc.* **2011**, *133*, 16414−16417.
(25) Suprabha, T.; Roy, H. Z.; Thomas, J.; Kumar, K. P.; Mathew, S. Microwave-Assisted Synthesis of Titania Nanocubes, Nanospheres and Nanorods for Photocatalystic Dye Degradation. *Nanoscale Res. Lett.* **2009**, *4*, 144−152.
(26) Zhu, J. F.; Zheng, W.; He, B.; Zhang, J. L.; Anpo, M. Characterization of Fe-TiO_2 Photocatalysts Synthesized by Hydrothermal Method and Their Photocatalytic Reactivitity for Photodegradation of XRG Dye Diluted in Water. *J. Mol. Catal. A: Chem.* **2004**, *216*, 35−43.
(27) Liao, Y. L.; Que, W. X.; Jia, Q. Y.; He, Y. C.; Zhang, J.; Zhong, P. Controllable Synthesis of Brookite/Anatase/Rutile Nanocomposites and Single-Crystalline Rutile Nanorods Array. *J. Mater. Chem.* **2012**, *22*, 7937−7944.
(28) Chuangchote, S.; Jitputti, J.; Sagawa, T.; Yoshikawa, S. Photocatalytic Activity for Hydrogen Evolution of Electrospun TiO_2 Nanofibers. *ACS Appl. Mater. Interfaces* **2009**, *1*, 1140−1143.
(29) Sarkar, D.; Ghosh, C. K.; Mukherjee, S.; Chattopadhyay, K. K. Three Dimensional Ag_2O/TiO_2 Type-II (p-n) Nanoheterojunctions for Superior Photocatalytic Activity. *ACS Appl. Mater. Interfaces* **2013**, *5*, 331−337.
(30) Liu, S. W.; Yu, J. G.; Jaroniec, M. Tunable Photocatalytic Selectivity of Hollow TiO_2 Microspheres Composed of Anatase Polyhedra with Exposed {001} Facets. *J. Am. Chem. Soc.* **2010**, *132*, 11914−11916.
(31) Ahmed, A. Y.; Kandiel, T. A.; Oekermann, T.; Bahnemann, D. Photocatalytic Activities of Different Well-defined Single Crystal TiO_2 Surface: Anatase versus Rutile. *J. Phys. Chem. Lett.* **2011**, *2*, 2461−2465.
(32) Zhang, H. M.; Wang, Y.; Liu, P. R.; Han, Y. H.; Yao, X. D.; Zou, J.; Cheng, H. M.; Zhao, H. J. Anatase TiO_2 Crystal Facet Growth: Mechanistic Role of Hydrofluoric Acid and Photoelectrocatalytic Activity. *ACS Appl. Mater. Interfaces* **2011**, *3*, 2437−2478.
(33) Liao, Y. L.; Zhang, H. W.; Que, W. X.; Zhong, P.; Bai, F. M.; Zhong, Z. Y.; Wen, Q. Y.; Chen, W. H. Activating the Single-Crystal TiO_2 Nanoparticle Film with Exposed {001} Facets. *ACS Appl. Mater. Interfaces* **2013**, *5*, 6463−6466.
(34) Lazzeri, M.; Vittadini, A.; Selloni, A. Structure and Energetics of Stoichiometric TiO_2 Anatase Surfaces. *Phys. Rev. B: Condens. Matter Mater. Phys.* **2001**, *63*, 155409.
(35) Xu, H.; Reunchan, P.; Ouyang, S. X.; Tong, H.; Umezawa, N.; Kako, T.; Ye, J. H. Anatase TiO_2 Single Crystals Exposed with High-Reactive {111} Facets Toward Efficient H_2 Evolution. *Chem. Mater.* **2013**, *25*, 405−411.
(36) Wu, X.; Chen, Z. G.; Lu, G. Q.; Wang, L. Z. Nanosized Anatase TiO_2 Single Crystals with Tunable Exposed (001) Facets for Enhanced Energy Conversion Efficiency of Dye-Sensitized Solar Cell. *Adv. Funct. Mater.* **2011**, *21*, 4167−4172.
(37) Wen, C. Z.; Zhou, J. Z.; Jiang, H. B.; Hu, Q. H.; Qiao, S. Z.; Yang, G. Y. Synthesis of Micro-sized Titanium Dioxide Nanosheets wholly Exposed With Highly-Energy {001} and {100} Facets. *Chem. Commun.* **2011**, *47*, 4400−4402.
(38) Wu, B. H.; Guo, C. Y.; Zheng, N. F.; Xie, Z. X.; Stucky, G. D. Nonaqueous Production of Nanostructured Anatase with High-Energy Facets. *J. Am. Chem. Soc.* **2008**, *130*, 17563−17567.
(39) Pan, J.; Liu, G.; Lu, G. Q.; Cheng, H. M. On the True Photoreactivity Order of {001}, {010}, and {101} Facets of Anatase TiO_2 Crystals. *Angew. Chem., Int. Ed.* **2011**, *50*, 2133−2137.
(40) Yang, W. G.; Wang, Y. L.; Shi, W. M. One-Step Synthesis of Single-Crystal Anatase TiO_2 Tetragonal Faceted-Nanorods for Improved-Performance Dye-Sensitized Solar Cells. *CrystEngComm* **2012**, *14*, 230−234.
(41) Pan, J.; Wu, X.; Wang, L.; Liu, G.; Lu, G. Q.; Cheng, H. M. Synthesis of Anatase TiO_2 Rods with Dominant Reactive {010} Facets for the Photoreduction of CO_2 to CH_4 and Use in Dye-Sensitized Solar Cells. *Chem. Commun.* **2011**, *47*, 8361−8363.
(42) Wen, P. H.; Itoh, H.; Feng, Q. Preparation of Nanoleaf-Like Single Crystals of Anatase-Type TiO_2 by Exfoliation and Hydrothermal Reactions. *Chem. Lett.* **2006**, *35*, 1226−1227.
(43) Wen, P. H.; Itoh, H.; Tang, W.; Feng, Q. Tranformation of Layered Titanate Nanosheets into Nanostructures Porous Titanium Dioxid in Polycation Solution. *Microporous Mesoporous Mater.* **2008**, *116*, 147−156.
(44) Wen, P. H.; Ishikawa, Y.; Itoh, H.; Feng, Q. Topotactic Tranformation Reaction from Layered Titanate Nanosheets into Anatase Nanocrystals. *J. Phys. Chem. C* **2009**, *113*, 20275−20280.
(45) Wen, P. H.; Itoh, H.; Tang, W. P.; Feng, Q. Single Nanocrystals of Anatase-Type TiO_2 Prepared from Layered Titanate Nanosheets: Formation Mechanism and Characterization of Surface Properties. *Langmuir* **2007**, *23*, 11782−11790.
(46) Wen, P. H.; Tao, Z. Q.; Ishikawa, Y.; Itoh, H.; Feng, Q. Dye-Sensitized Solar Cells Based on Anatase TiO_2 Nanocrystals Exposing a Specific Lattice Plane on the Surface. *Appl. Phys. Lett.* **2010**, *97*, 131906.
(47) Tanaka, B. T.; Fukuda, K.; Ebina, Y.; Takada, K.; Sasaki, T. Highly Organized Self-Assemble Monolayer and Multilayer Films of Titania Nanosheets. *Adv. Mater.* **2004**, *16*, 872−875.
(48) Feng, Q.; Kajiyoshi, K.; Yanagisawa, K. Topotactic Preparation of Preferentially Oriented $BaTiO_3$ and TiO_2 Thin Films on Polycrystalline Substrate. *Chem. Lett.* **2003**, *32*, 48−49.
(49) Yin, S.; Sato, T. Synthesis and Photocatalytic Properties of Fibrous Titania Prepared from Protonic Layered Tetratitanate Precursor in Supercritical Alcohols. *Ind. Eng. Chem. Res.* **2000**, *39*, 4526−4530.
(50) Shen, L. M.; Bao, N. Z.; Zheng, Y. Q.; Gupta, A.; An, T. C.; Yanagisawa, K. Hydrothermal Splitting of Titanate Fibers to Single-Crystalline TiO_2 Nanostructures with Controllable Crystalline Phase, Morphology, Microstructure, and Photocatalytic Activity. *J. Phys. Chem. C* **2008**, *112*, 8809−8818.
(51) Wang, J. S.; Li, H. Y.; Wang, H.; Huang, K. L.; Sun, G. S.; Yin, S.; Sato, T. Morphology Control of TiO_2 through Hydrothermal Synthesis Method Using Protonic Tetratitanate. *Res. Chem. Intermed.* **2011**, *37*, 165−175.
(52) Izawa, H.; Kikkawa, S.; Koizumi, M. Ion Exchange and Dehydration of Layered Titanate, $Na_2Ti_3O_7$ and $K_2Ti_4O_9$. *J. Phys. Chem.* **1982**, *86*, 5023−5026.
(53) Yu, L.; Yuan, S.; Shi, L. Y.; Zhao, Y.; Fang, J. H. Synthesis of Cu^{2+} Doped Mesoporous Titania and Investigation of Its Photocatalytic Ability under Visible Light. *Microporous Mesoporous Mater.* **2010**, *134*, 108−114.
(54) Allen, M. R.; Thibert, A.; Sabio, E. M.; Browning, N. D.; Larsen, D. S.; Osterloh, F. E. Evolution of Physical and Photocatalytic Properties in the Layered Titanates $A_2Ti_4O_9$ (A = K, H) and

Nanosheets Derived by Chemical Exfoliation. *Chem. Mater.* **2010**, *22*, 1220−1228.
(55) Suzuki, S.; Miyayama, M. Lithium Intercalation Properties of Octatitanate Synthesized through Exfoliation/ Reaseembly. *J. Phys. Chem. B* **2006**, *110*, 4731−4734.
(56) Sugimoto, W.; Terabayashi, O.; Murakami, Y.; Takasu, Y. Electrophoretic Deposition of Negatively Charged Tetratitanate Nanosheets and Transformation into Preferentially Oriented TiO_2(B) Film. *J. Mater. Chem.* **2002**, *12*, 3814−3818.
(57) Wang, J. F.; Zhu, G.; Deng, L. J.; Kang, L. P.; Hao, Z. P.; Liu, Z. H. Novel Synthesis and Formation Process of Uniform Mn_2O_3 Cubes. *CrystEngComm* **2012**, *14*, 8253−8260.
(58) Cheng, S.; Wang, T. Pillaring of Layered Titanates by Polyoxo Cations of Aluminum. *Inorg. Chem.* **1989**, *28*, 1283−1289.
(59) Li, X. K.; Yue, B.; Ye, J. H. Photocatalytic Hydrogen Evolution over SiO_2-Pillared and Nitrogen-Doped Titanic Acid under Visible Light Irradiation. *Appl. Catal., A* **2010**, *390*, 195−200.
(60) Maireles-Torres, P.; Olivera-Pastor, P.; Rodriguez-Castellon, E.; Jimenez-Lopez, A.; Alagna, L.; Tomlinson, A. A. G. Porous Cross-linked Materials Formed by Oligometric Aluminium Hydroxide and α-Tin Phosphate. *J. Mater. Chem.* **1991**, *1*, 319−326.
(61) Hou, W. H.; Chen, Y. S.; Guo, C. X.; Yan, Q. J. Synthesis of Porous Chromia-Pillared Tetratitanate. *J. Solid State Chem.* **1998**, *136*, 320−321.
(62) Manseki, K.; Kondo, Y.; Ban, T.; Sugiura, T.; Yoshida, T. Size-Controlled Synthesis of Anisotropic TiO_2 Single Nanocrystals Using Microwave Irradiation and Their Application for Dye-Sensitized Solar Cells. *Dalton Trans.* **2013**, *42*, 3295−3299.
(63) Howard, C. J.; Sabine, T. M.; Dickson, F. Structural and Thermal Parameters for Rutile and Anatase. *Acta Crystallogr., Sect. B* **1991**, *47*, 462−468.
(64) Challa, S. R.; Delariva, A. T.; Hasen, T. W.; Helveg, S.; Sehested, J.; Hasen, P. L.; Garzon, F.; Datye, A. K. Relating Rates of Catalyst Sintering to the Disappearance of Individual Nanoparticles during Oswald Ripening. *J. Am. Chem. Soc.* **2011**, *133*, 20672−20675.
(65) Momma, K.; Izumi, F. VESTA 3 for Three-Dimensional Visualization of Crystal, Volumetric and Morphology Data. *J. Appl. Crystallogr.* **2011**, *44*, 1272−1276.
(66) *Nano Measurer (Particle Size Distribution Calculation Software)*; obtained from Department of Chemistry, Fudan University: Shanghai, China.
(67) Cullity, B. D. *Elements of X-Ray Diffraction*; Addison−Wesley: Reading, MA, 1978.
(68) Feng, Q.; Hirasawa, M.; Yanagisawa, K. Synthesis of Crystal-Axis-Oriented $BaTiO_3$ and Anatase Platelike Particles by a Hydrothermal Soft Chemical Progress. *Chem. Mater.* **2001**, *13*, 290−296.
(69) Zhao, J.; Zou, X.-X.; Su, J.; Wang, P.-P.; Zhou, L.-J.; Li, G.-D. Synthesis and Photocatalystic Activity of Porous Anatase TiO_2 Microspheres Compose of {010}-facet Nanobelt. *Dalton Trans.* **2013**, *42*, 4365−4368.
(70) Xue, M.; Chitrakar, R.; Saknane, K.; Hirotsu, T.; Ooi, K.; Yoshimura, Y. J.; Feng, Q.; Sumida, N. Selective Adsorption of Thiophene and 1-Benzothiophene on Metal-Ion-Exchanged Zeolites in Organic Medium. *J. Colloid Interface Sci.* **2005**, *285*, 487−492.
(71) Wen, P. H.; Xue, M.; Ishikawa, Y.; Itoh, H.; Feng, Q. Relationships between Cell Parameters of Dye-Sensitized Solar Cells and Dye-Adsorption Parameters. *ACS Appl. Mater. Interfaces* **2012**, *4*, 1928−1934.
(72) Takahashi, J. Dye Adsorption Behavior of Anatase- and Rutile-Type TiO_2 Nanoparticles Modified by Various Heat-Treatments. *J. Mater. Sci.* **2003**, *38*, 1695−1702.
(73) Tan, B.; Wu, Y. Y. Dye-Sensitized Solar Cells Based on Anatase TiO_2 Nanoparticle/Nanowire Composites. *J. Phys. Chem. B* **2006**, *110*, 15932−15938.
(74) Wang, Z.-S.; Kawauchi, H.; Kashima, T.; Arakawa, H. Significant Influence of TiO_2 Photoelectrode Morphology on the Energy Conversion Efficiency of N719 Dye-Sensitized Solar Cell. *Coord. Chem. Rev.* **2004**, *248*, 1381−1389.
(75) Neale, N. R.; Kopidakis, N.; van de Lagemaat, J.; Grätzel, M.; Frank, A. J. Effect of a Coadsorbent on the Performance of Dye-Sensitized TiO_2 Solar Cells: Shielding versus Band-Edge Movement. *J. Phys. Chem. B* **2005**, *109*, 23183−23189.
(76) Meng, Q. B.; Takahashi, K.; Zhang, X. T.; Sutanto, I.; Rao, T. N.; Sato, O.; Fujishima, A. Fabrication of an Efficient Solid-State Dye-Sensitized Solar Cell. *Langmuir* **2003**, *19*, 3572−3574.
(77) Zhao, N.; Osedach, T. P.; Chang, L.-Y.; Gryer, S. M.; Wanger, D.; Binda, M. T.; Arango, A. C.; Bawendi, M. G.; Bulovic, V. Colloidal PbS Quantum Dot Solar Cells with High Fill Factor. *ACS Nano* **2010**, *4*, 3743−3752.